




# Facile, low cost synthesis of cauliflower-shaped ZnO with MWCNT/rGO nanocomposites and their photocatalytic activity

V. Arun<sup>1,3</sup>, S. Prabhu<sup>2</sup>, A. Priyadharsan<sup>3</sup>, P. Maadeswaran<sup>1,\*</sup> , S. Sohila<sup>4</sup>, R. Ramesh<sup>2</sup>, and A. Senthil Kumar<sup>5</sup>

<sup>1</sup>Department of Energy Science, Periyar University, Salem, Tamil Nadu 636011, India

<sup>2</sup>Department of Physics, Periyar University, Salem, Tamil Nadu 636011, India

<sup>3</sup>Department of Physics, E.R.K Arts and Science College, Erumiyampatti, Dharmapuri, Tamil Nadu 636905, India

<sup>4</sup>Department of Physics, Padmavani Arts and Science College for Women, Salem, Tamil Nadu 636011, India

<sup>5</sup>Department of Physics, PSG College of Technology, Coimbatore, Tamil Nadu 641 004, India

**Received:** 11 November 2020

**Accepted:** 4 May 2021

**Published online:**

17 May 2021

© The Author(s), under exclusive licence to Springer Science+Business Media, LLC, part of Springer Nature 2021

## ABSTRACT

The present work reports cauliflower-shaped ZnO nanostructure, and ZnO/multi-wall carbon nanotubes/rGO (ZMG NCs) nanocomposites were synthesized by surfactant-assisted simple hydrothermal method. The structural, morphological, optoelectronic, chemical state, surface properties and its photocatalytic capability were performed using various analytical techniques. The UV–Vis DRS results revealed that optical absorption of ZMG NCs was red shifted into visible region. Furthermore, the photocatalytic removal of methylene blue (MB) dye in aqueous solution was performed using the resulting catalysts, achieves maximum degradation efficiency of 96.3% under UV–Vis light irradiation for 25 min as compared with ZnO/MWCNT (86.01%), ZnO/rGO (79.6%), and ZnO (71.9%). The enhancement in the photocatalytic degradation efficiency of ZMG NCs was attributed to the red-shifted band gap (2.89 eV) and high surface area (45.877 m<sup>2</sup> g<sup>-1</sup>). Moreover, the ZMG ternary NCs possessed good chemical stability, and it has a great potential application for photocatalytic dye degradation and wastewater treatment.

V. Arun and S. Prabhu made equal contribution.

Address correspondence to E-mail: maadeswaranp@periyaruniversity.ac.in; rameshphys@gmail.com

<https://doi.org/10.1007/s10854-021-06129-5>

## 1 Introduction

Owing to the rapid globalization and industrialization, energy crisis and environmental effluence were major concerns and thus pursuing for renewable and clean energy sources [1]. In that manner, waste water contaminant is a hot issues since water is a major resource of all beings from aquatic, humans and all other living organisms [2]. Therefore, various industry sectors like leather, textile, paper and pharma produce a large amount of wastewater containing a mixture of organic contaminants, heavy metal ions, and long-chain polymer which causes diseases when it is reused without appropriate purification [3]. Hence, purification of water by-products from the textile industry (in particular dye molecules) is highly crucial for a clean and green environment. However, several approaches have been used to remove the contamination of wastewater treatment including ion-exchange, sonocatalysis, membrane filtration, reverse osmosis, photocatalysis, and photoelectrochemical water splitting [4–9]. Among these methods, photocatalysis provides great assistances to agreement with the environmental challenges and sustainability with solar light. In recent researches, ZnO acts as an n-type semiconductor with bandgap energy of 3.37 eV, extensively investigated as the most active photocatalyst [10, 11]. Hence, charge trapping at the surface of catalyst is essential to restrict carrier recombination, and to attain efficient photocatalysis. Recombination has faster kinetics than surface redox reactions and greatly reduces the quantum efficiency of photocatalysis [12–14]. Currently, an attractive option is to design, develop doping and composite materials based on ZnO to solve this problem.

Carbon-based nanomaterials, such as activated carbon (AC), graphene oxides (GO), carbon nanofibers (CNF), and carbon nanotubes (CNT), have widely used in optoelectronics, catalysis, sensing, and supercapacitors due to its high energy transformation [15–18]. The reduced graphene oxide (rGO) exhibits reactive oxygen functional groups on the sheet surface (carboxylic acid, hydroxyl, and epoxide groups) [19–21]. Moreover, the rGO exhibits good thermal, chemical stability, and more conducting property [22]. It acts as an electron-acceptor and as an electron-transport mediator; hence, it will facilitate the migration of photoinduced electrons and hinder

the charge recombination to enhance the photocatalytic performance [23]. In a previous report, Z. Chen et al. synthesized graphene-ZnO nanorod nanocomposites via a facile hydrothermal method and investigated their photocatalytic performance in the degradation of methylene blue (MB) within 40 min under ultraviolet (UV) light irradiation [24]. A. Shanmugasundaram et al. reduced graphene oxide-zinc oxide (rGO/ZnO) composites via a facile hydrothermal route, which demonstrated enhanced photocatalytic activity toward MB degradation (98%) [25]. D. Shao et al. thorn-like ZnO/MWCNT composite was synthesized by hydrothermal synthesis, whereas degradation of RhB (98%) with 90 min under UV light irradiation [26]. T. A Saleh et al. demonstrate the zinc oxide was loaded onto multi-walled carbon nanotubes (MWCNTs) via a hydrothermal method and photocatalytic activity in the removal of highly toxic substances like cyanide (CN) under the laser irradiation at 40 min [27]. There are several chemical synthesis methods undertaken for the preparation of ZnO/MWCNT/rGO nanocomposites such as solid-state reaction [28], solution combustion [29], sol-gel [30], co-precipitation method [31], hydrothermal [32], solvothermal [33] and sonochemical [34]. Among these methods, the surfactant-assisted hydrothermal method is one of the cost-effective approaches to synthesize nanocomposite materials, which is a high purity, well-crystallized, homogeneous chemical structures and more active surface area [35, 36].

In the present work, cauliflower-shaped ZnO, ZnO/rGO, ZnO/MWCNT, and ZnO/MWCNT/rGO (ZMG NCs) nanocomposites were synthesized by surfactant-assisted hydrothermal method. The photophysical properties of the structural, morphological, optical, chemical state, and surface area of the samples were investigated through XRD, FE-SEM, HR-TEM, UV-Vis DRS, FT-IR, XPS, and BET, respectively. The photocatalytic performance of the resultant bare, binary, and ZMG ternary NCs was investigated by removal of methylene blue MB dye in the aqua solution. The enhanced photocatalytic activity of ZMG NCs (96% within 25 min) and the introduced MWCNT and rGO improved the charge separation, transportation, and visible light response of the ZnO. It was demonstrated that the stability test of ZMG NCs over a repeated 5 cycles of dye degradation does not affect XRD pattern.

## 2 Experimental section

### 2.1 Chemicals

Zinc acetate dihydrate ( $(\text{Zn}(\text{CH}_3\text{COO})_2 \cdot 2\text{H}_2\text{O})$ —99%, Loba Chemie), multiwalled carbon nanotubes ((MWCNT) 98.5%, length (1 to 10  $\mu\text{m}$ )), graphite powder (98%, Loba Chemie), potassium permanganate ( $(\text{KMnO}_4)$  99%, Loba Chemie), sodium nitrate ( $(\text{NaNO}_3)$ -99%, Sigma-Aldrich), hydrogen peroxide ( $(\text{H}_2\text{O}_2)$  30%, Emparta), sulfuric acid ( $(\text{H}_2\text{SO}_4)$  98%, Loba Chemie), diethylenetriamine ( $(\text{C}_6\text{H}_{15}\text{N})$  99%, Merck) and dodecylamine ( $(\text{C}_{12}\text{H}_{27}\text{N})$ -99%, Merck) were used. All the chemicals were purchased commercially and used as without further purification.

### 2.2 Synthesis of cauliflower-shaped ZnO nanoparticles

The cauliflower structured ZnO nanoparticles were synthesized through the mixed amine-based hydrothermal method. In our previous work, we have briefly given the synthesis in single amine-based various shape and size-controlled morphology [8, 10, 32]. In a typical synthesis, 3.51 g of zinc acetate dihydrate (0.2 M) was dissolved into 80 mL of distilled water under magnetic stirring. 5 mL of diethylenetriamine and 5 mL of dodecylamine were dropwise added into the above solution, and the white precipitate was formed. The precipitate was transferred into an autoclave and heated at 200 °C for 12 h in a hot air oven. When the autoclave was naturally cooled at room temperature. In our preparation method, surfactants (mixed amine diethylenetriamine and dodecylamine) were used as morphology controlling agents with autoclave-assisted hydrothermal synthesis (high temperature and pressure) without an additional calcination step which offers the feasibility for obtaining the pure phase and the desired nanostructure simultaneously that form a ZnO cauliflower-like nanostructures. The obtained precipitation was washed with distilled water and ethanol several times, and the product was filtered. Finally, filtered product was dried at 80 °C in a hot air oven for 12 h to obtain cauliflower-shaped ZnO nanoparticles.

### 2.3 Preparation of ZnO/rGO, ZnO/MWCNT and ZMG NCs

The ZnO/rGO, ZnO/MWCNT, and ZMG NCs were prepared by the hydrothermal method as follows. The synthesis of rGO was the same procedure based on previously reported work [9]. As-prepared rGO (100 mg) was dispersed by ultrasonication for 3 h and then transferred into 80 mL deionized water. After that, 3.51 g of zinc acetate dihydrate was dissolved into the above solution under magnetic stirring. Then, 5 mL of diethylenetriamine and dodecylamine were slowly added in the above solution. The mixture was transferred into an autoclave and heated constant temperature at 200 °C for 12 h. After the reaction was cooled to room temperature, the product was filtered and dried at 80 °C in an air-driven hot oven to obtain the final ZnO/rGO nanocomposites.

As-purchased multiwalled carbon nanotubes (MWCNT) 100 mg was dispersed into 80 mL deionized water with ultrasonication for 2 h. After that, 3.51 g of zinc acetate dihydrate was dissolved above mixture under magnetic stirring. The diethylenetriamine (5 mL) and dodecylamine (5 mL) were added dropwise in the above solution. The resulting solution was transferred into stainless steel lined autoclave and heated constant temperature at 200 °C for 12 h. Afterward, the autoclave was cooled to room temperature, and the product was filtered and dried at 80 °C in overnight.

In a typical synthesis, an equal amount (1:1) of rGO (100 mg) and MWCNT (100 mg) was suspended in 80 mL of distilled water using ultrasonic waves until it turned to a block homogeneous solution. 3.51 g of zinc acetate dihydrate, diethylenetriamine (5 mL), and dodecylamine (5 mL) were added to the above suspension with magnetic stirring for 1 h. The resultant mixture was transferred into Teflon lined autoclave and heated at 200 °C for overnight. During hydrothermal treatment the chemically interacted amines are mixed with the optimized materials. So that the surface is functionalized and reduced for the possibilities of amines covered on the surfaces. Finally, the product was centrifuged, washed with ethanol, water several times, and dried at 80 °C for 12 h in a hot air oven to obtain the ZMG NCs.

## 2.4 Characterizations

The powder X-ray diffraction (XRD) patterns of the hydrothermally prepared nanocomposite were characterized by an X-ray diffractometer (Rigaku-CuK $\alpha$  radiation source ( $\lambda = 0.154$  nm) operated at 40 kV). Internal and surface morphology of the prepared nanocomposite was visualized through a high-resolution transmission electron microscope (HRTEM, Hitachi H-600 operated at 200 kV) and field emission scanning electron microscope (FESEM, Hitachi S-4800). The optical properties of the synthesized samples were measured by a UV–Vis diffuse reflectance spectrophotometer (DRS, PerkinElmer, Lambda-1050). The vibration modes of the catalysts were investigated through the FT-IR technique with a range of 4000 to 400  $\text{cm}^{-1}$  (FT-IR, NEXUS 470). The surface area of the obtained samples was characterized under the Brunauer–Emmett–Teller analysis (BET, Micromeritics, ASAP-2020, USA). The chemical states of the samples were identified X-ray photoelectron spectroscopy technique (XPS, ESCA 3400 spectrometer).

## 2.5 Photocatalytic measurements

The photocatalytic activity of the prepared products was examined for the degradation of methylene blue (MB) aqua solution under UV–visible light irradiation at room temperature. Typically, 100 mg (1 g/L) of ZMG NCs was suspended in 100 mL aqueous solution of MB (10 mg/L). Before light illumination, the solution was continuously stirred under the dark condition for 2 h to reach adsorption–desorption equilibrium. The MB dye solution had constant pH levels of 7, which was adjusted using diluted HCl/NaOH solutions. Then, the mixture was irradiated by halogen lamp (Philips G6.35 Bi-Pin-250 W) with 20 cm distance from the photoreactor (it was made in the home) to start the photocatalytic experiment at the regular time interval (5 min); 2 mL solution was taken, and separate to centrifuge at 10,000 rpm. After that, the concentration of dye molecules was measured from the JASCO V-670 UV–Vis absorbance spectra. Furthermore, evaluate accuracy in ZMG NCs, the photocatalytic process was reused five times to degrade MB dye under visible light irradiation. The dye degradation efficiency (%) was calculated using the following equation [37]:

$$\eta = \frac{A_0 - A}{A_0} \times 100\% \quad (1)$$

where  $A_0$  is the concentration of dye before irradiation and  $A$  is the concentration of dye after photoirradiation.

## 2.6 Determination of active species

The reactive photocatalytic active species were investigated by above photocatalytic experiment. The various active species were superoxide ( $\text{O}_2^{\cdot-}$ ), hydroxyl (OH), holes ( $\text{h}^+$ ), and electrons ( $\text{e}^-$ ). In order to study the role of active substance including electrons ( $\text{e}^-$ ), holes ( $\text{h}^+$ ),  $\cdot\text{OH}$  and  $\text{O}_2^{\cdot-}$  during the process of catalytic reaction, 1 mmol of benzoquinone (BQ), isopropanol (IPA), triethanolamine (TEOA) and silver nitrate ( $\text{AgNO}_3$ ) were added into 100 mL MB solution as electron, hole,  $\cdot\text{OH}$  and  $\text{O}_2^{\cdot-}$  sacrificial agents, respectively [38].

## 2.7 Photoelectrochemical experiments

Transient photocurrent (i-t) and electrochemical impedance (EIS) measurements were investigated by BioLogic SP-150 electrochemical workstation using a three-electrode system performed in 0.5 M  $\text{Na}_2\text{SO}_4$  electrolyte solution. In the three-electrode system, Ag/AgCl (saturated KCl solution) acts as a reference electrode, platinum plate acts as a counter electrode, and prepared sample was the working electrode. The preparation of working electrode is as follows: 10 mg of ZMG NCs were dispersed in the 1 mL of ethanol and 25  $\mu\text{L}$  Nafion solution with ultrasonication for 30 min. The ultrasonicated solution was deposited on the FTO glass substrate by spin coating method (spin coater model No: HO-TH-05) with rpm speed above 2000 rpm for 5 min. The spin coated working electrodes were dried at 60  $^\circ\text{C}$  under a hot air oven. In this experiment, the xenon lamp (150 W) was used as a light source to illuminate by the working electrode surfaces (power intensity 100  $\text{mW}/\text{cm}^2$ ). Moreover, the EIS studies were performed in the AC amplitude of 5 mV at open-circuit potential with an applied frequency ranging from 0.001 Hz to 100 kHz.

### 3 Results and discussion

#### 3.1 Powder XRD analysis

The phase purity and crystal structure of the synthesized samples were characterized by powder X-ray diffraction (XRD) technique. Figure 1 shows the XRD patterns of rGO, MWCNT, cauliflower-shaped ZnO, ZnO/rGO, ZnO/MWCNT and ZMG NCs. Figure 1a shows a broad diffraction peak appeared at  $2\theta = 26.2^\circ$ , which is corresponding to the (002) plane (hexagonal phase) of rGO with JCPDS no.75-1621. In Fig. 1b, the peak is observed at  $2\theta = 26.2^\circ$  for MWCNT, which can be attributed to the same plane value of rGO (002) with hexagonal structures (JCPDS no.75-1621). Figure 1c shows that ZnO diffraction peaks of  $2\theta$  values are  $31.9^\circ$ ,  $34.3^\circ$ ,  $36.2^\circ$ ,  $47.6^\circ$ ,  $56.6^\circ$ ,  $62.8^\circ$ ,  $67.8^\circ$  and  $69.2^\circ$  for the (100), (002), (101), (102), (110), (103), (112) and (201) planes with the hexagonal wurtzite structure (JCPDS No. 36-1451) [39]. The peak of rGO and MWCNT was detected, and the low content of rGO and MWCNT in the ZnO/rGO and ZnO/MWCNT nanocomposite appeared at  $2\theta = 26.2^\circ$  in Fig. 1d and e. The presence of rGO and MWCNT in the ZMG NCs is well clearly observed in Fig. 1e, in the  $2\theta$  range  $2\theta = 26.2^\circ$ . In

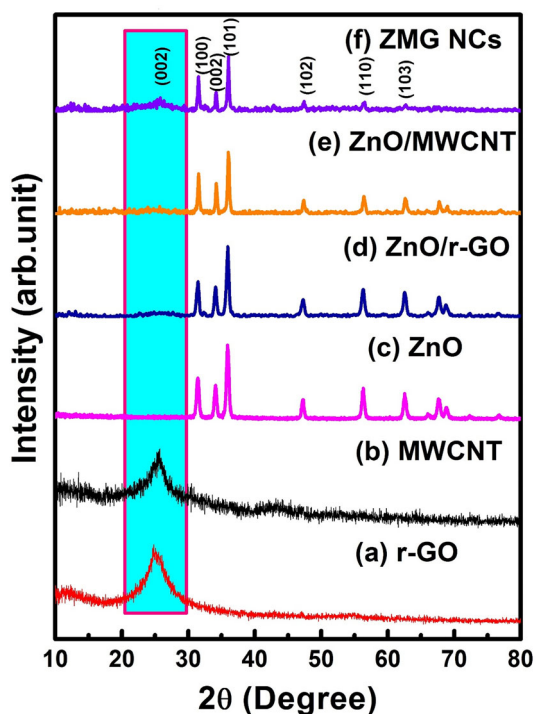


**Fig. 1** Powder XRD patterns of (a) rGO (b) MWCNT, (c) ZnO, (d) ZnO/rGO, (e) ZnO/MWCNT and (f) ZMG NCs

addition, to the diffraction peak from cauliflower-shaped ZnO, ZnO/rGO, ZnO/MWCNT and ZMG NCs indicate that the good crystallinity and no other impurities were present in all the synthesized samples.

#### 3.2 XPS analysis

The chemical states and surface elemental composition of the ZMG NCs were identified using the XPS technique. Survey spectrum of ZMG NCs in Fig. 2a shows the presence of C1s, O1s, Zn 2P<sub>3/2</sub> and Zn 2P<sub>1/2</sub> elements. Figure 2b shows the C1s high-resolution spectrum of ZMG NCs which using Gaussian method were deconvoluted into three peaks attributed to sp<sup>3</sup> hybridized C–C, C–O and C=O which correspond to the binding energies of 284.1 eV, 285.0 eV and 287.3 eV, respectively [40, 41]. This indicates that the oxygen in ZnO and in C=O has lower binding energy than the oxygen in C–O [42]. As shown in Fig. 2c, the O1s high-resolution spectra show three peaks at 531.1 eV, 532.2 eV and 533.1 eV for the O<sup>2-</sup> ions (wurtzite-type ZnO), OH and O<sub>2</sub>/OH [40]. The Zn 2p region shows a doublet (Fig. 2d) at Zn 2p<sub>3/2</sub> and Zn 2p<sub>1/2</sub> corresponding to binding energies of 1023.4 eV and 1046.2 eV for the ZnO/MWCT/rGO nanocomposite, respectively [43, 44]. These peaks were confirmed to the Zn<sup>2+</sup> oxidation state.

#### 3.3 FE-SEM analysis

The field emission scanning electron microscopy (FE-SEM) images were identified as the surface morphology of the obtain products. Figure 3a and b shows the ZnO cauliflower-like nanostructure, and the length, diameter values correspond to ~ 300–400 nm, and ~ 200–250 nm, respectively. From Fig. 3c and d, it is clearly seen that cauliflower ZnO nanostructures were uniformly dispersed on the rGO surfaces. The cauliflower-shaped ZnO was surrounded onto MWCNT with a unique structure in Fig. 3e and f. Moreover, Fig. 3f and g illustrates the cauliflower-shaped ZnO successfully incorporated into plate-like structure of rGO and MWCNT in the ZMG NCs. The EDS spectrum indicates that the marked area in Fig. S1 contains atomic and weight percentage of ZMG NCs, respectively.

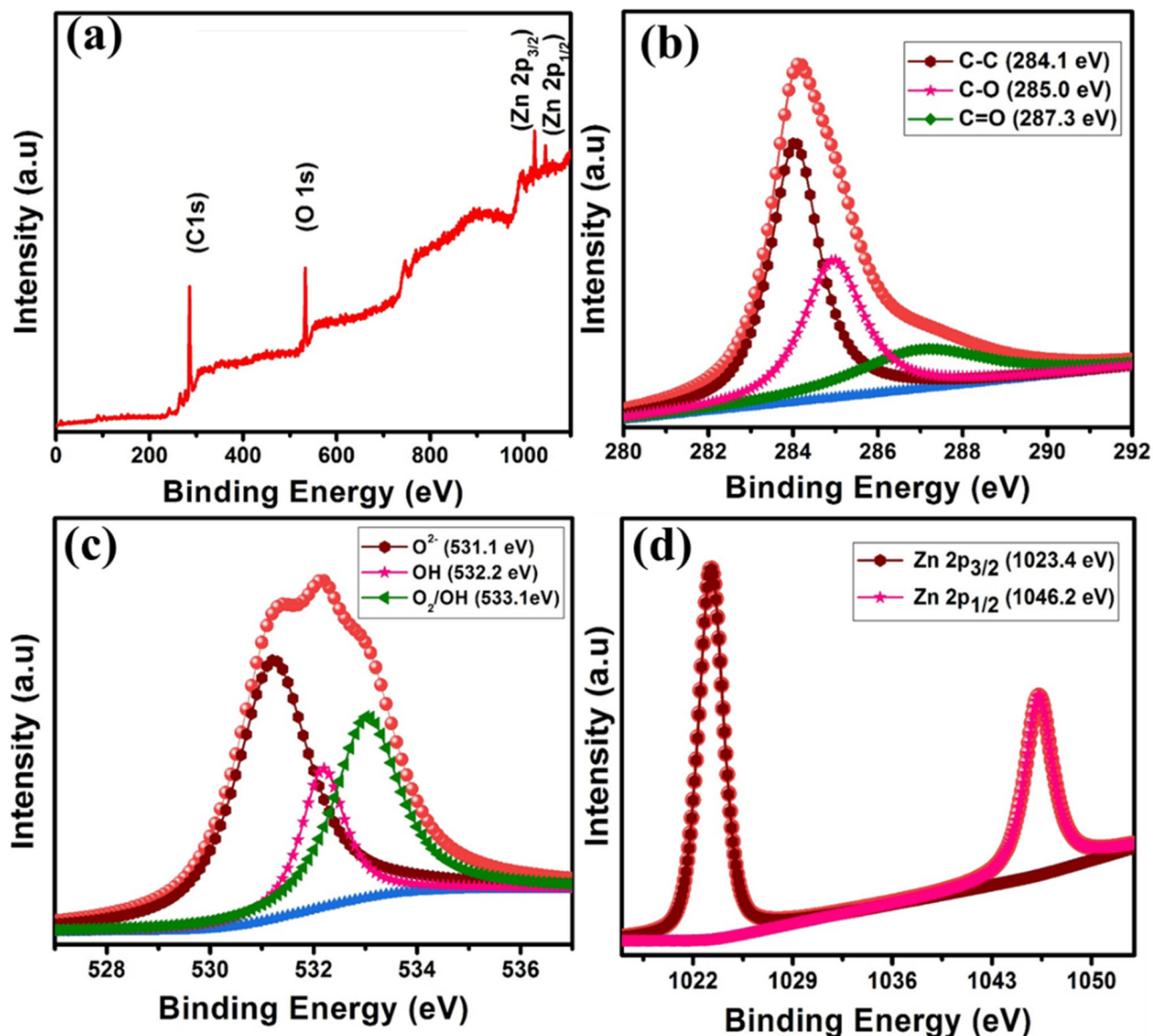


Fig. 2 XPS spectrum of the ZMG NCs samples: a survey spectrum, b C1s, c O1s and d Zn2p

### 3.4 TEM analysis

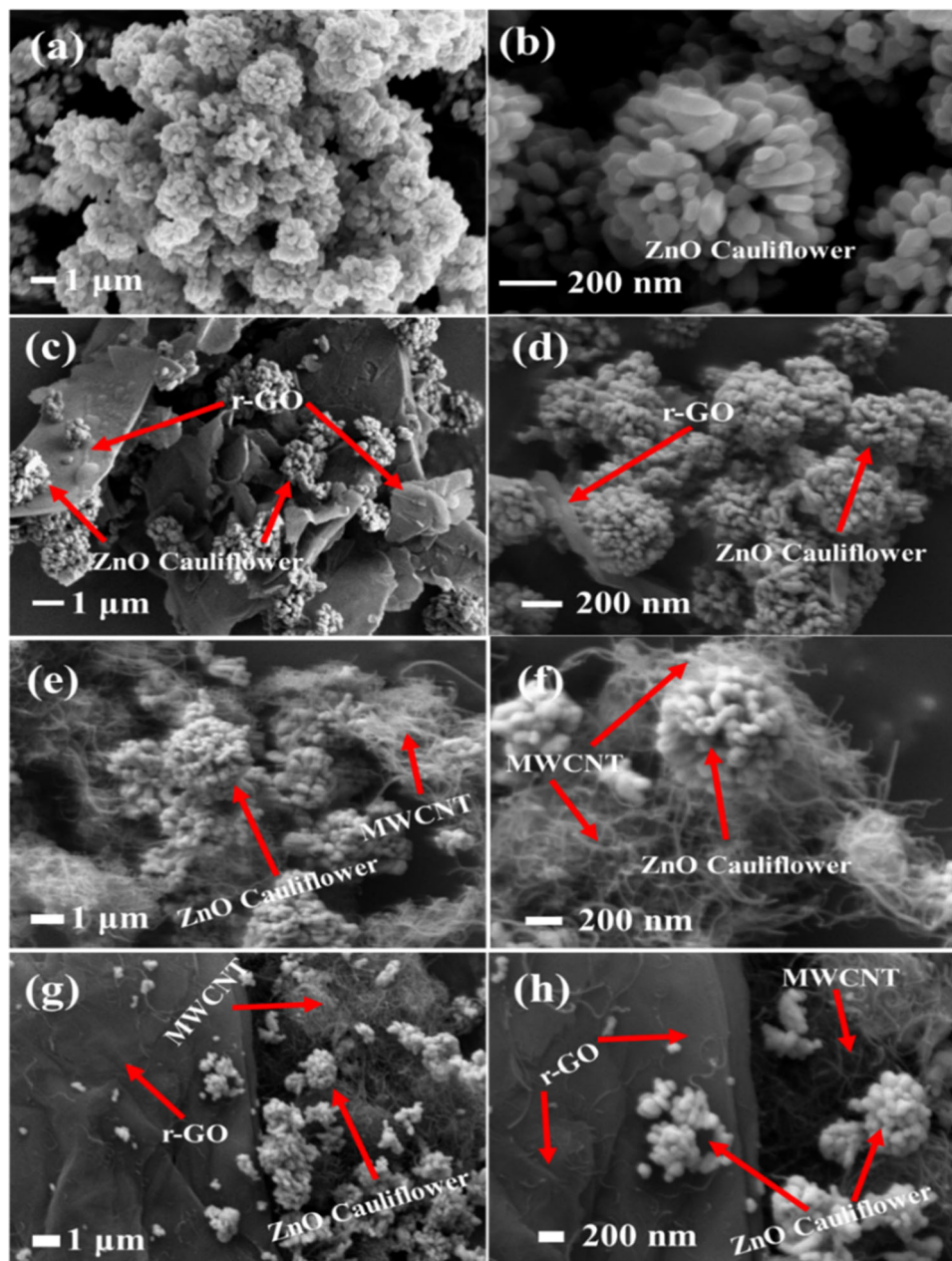
The detailed information on the internal morphology and structures of prepared samples was further confirmed by TEM and HR-TEM techniques. Figure 4a shows the monodispersed cauliflower morphology of the ZnO. The inter-planar spacing of 0.25 nm corresponds to the plane (0001), which is correlated with the hexagonal phase of ZnO in Fig. 4b. The TEM image of the ZMG NCs in Fig. 4c clearly visualized that the cauliflower ZnO nanostructures were surrounded by MWCNT and rGO sheets. Figure 4d shows the HR-TEM image

exhibited the cauliflower ZnO nanostructure and stacking of rGO layers with MWCNT and the calculated lattice d-spacing of 0.24 nm for the (0002) plane of the ZnO [45, 46]. Moreover, this results indicate the interfacial contact between ZnO, MWCNT, and rGO sheet with enhancing charge carrier transfer of dye degradation process.

### 3.5 BET analysis

Figure 5 shows the N<sub>2</sub> absorption–desorption isotherm and pore size distribution of the prepared ZnO and ZMG NCs. Both samples exhibited type-III N<sub>2</sub>

**Fig. 3** FE-SEM images of a–b cauliflower-shaped ZnO, c–d ZnO/rGO, e–f ZnO/MWCNT, g–h ZMG NCs



adsorption–desorption isotherms according to the Brunauer–Dening–Dening–Teller (BDDT) classification. While the nitrogen-adsorption curves of cauliflower-shaped ZnO and ZMG NCs show mesoporous nature, the BET specific surface area of cauliflower-shaped ZnO ( $8.200 \text{ m}^2 \text{ g}^{-1}$ ) is higher than that of ZMG NCs ( $45.877 \text{ m}^2 \text{ g}^{-1}$ ), mainly due to the MWCNT and graphene layer coated on the ZnO surfaces. The average pore size distribution is around 4.708 nm and 18.706 nm for the ZnO and ZMG NCs. The surface area of ZMG NCs was five times higher than cauliflower-shaped ZnO. The synergistic effect

of the combination of these materials combined with the preferential electro-reduction of GO gives rise to these remarkable values of ZMG NCs. Moreover, we have expected that high surface area by adsorbing a higher amount of organic dye molecules on the surface of ZMG NCs [47].

### 3.6 FT-IR analysis

The chemical structure and vibration modes of the prepared catalysts were investigated by the FT-IR measurement. Figure 6 shows the FT-IR spectra of

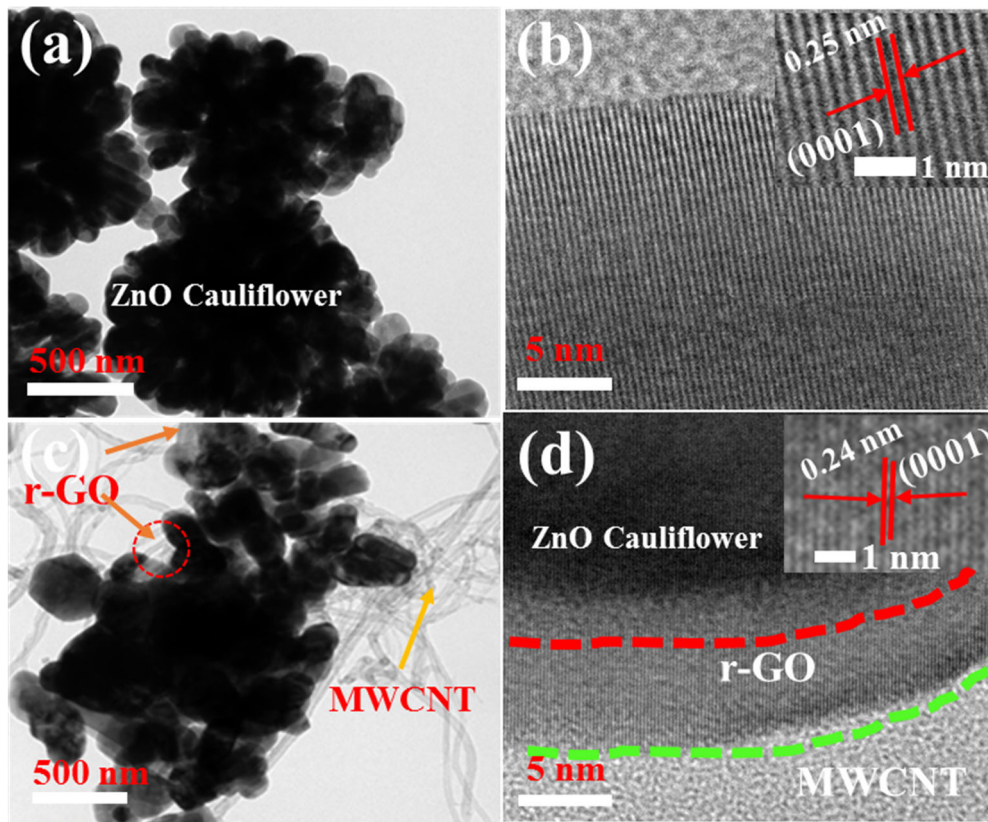


Fig. 4 TEM and HR-TEM images of a–b cauliflower-shaped ZnO and c–d ZMG NCs

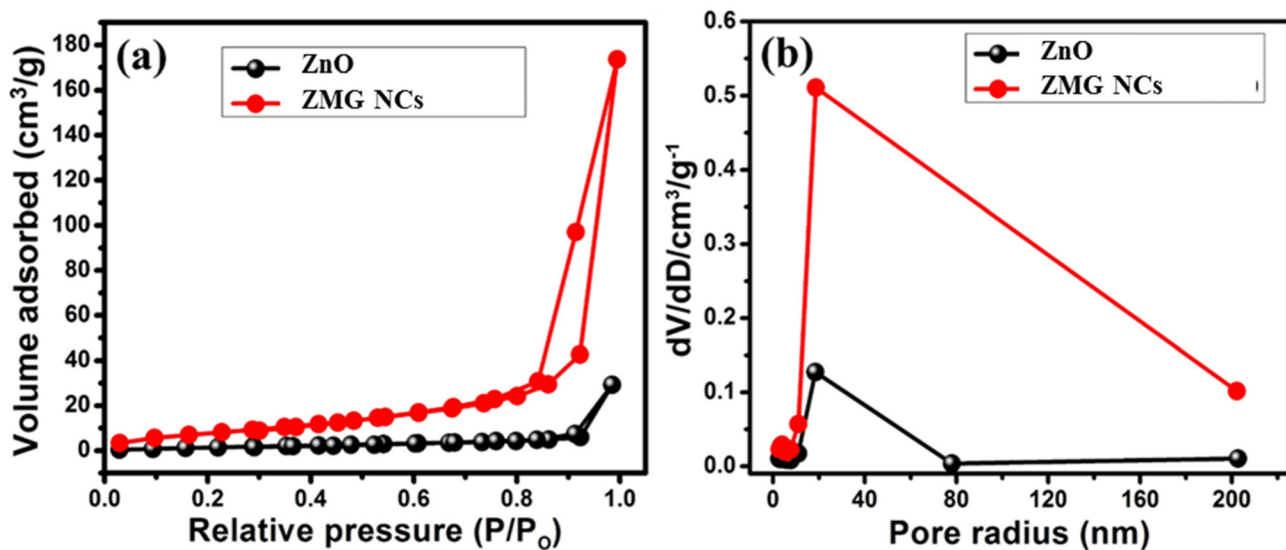
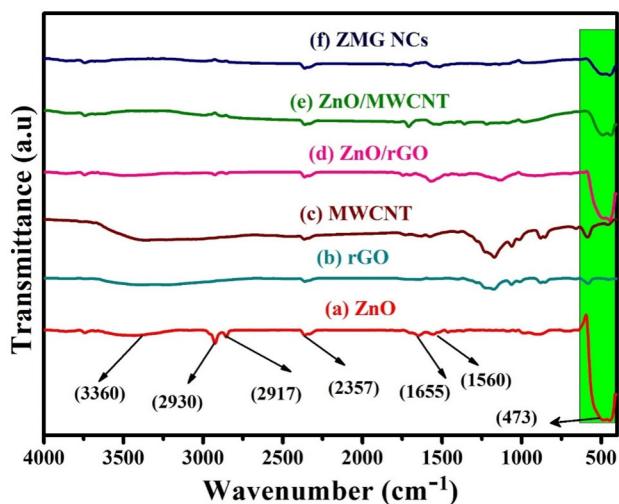


Fig. 5 a  $N_2$  adsorption–desorption isotherm and b pore distribution of cauliflower-shaped ZnO and ZMG NCs

cauliflower-shaped ZnO, rGO, MWCNT, ZnO/rGO, ZnO/MWCNT, and ZMG NCs in the range of  $4000\text{--}400\text{ cm}^{-1}$  recorded at room temperature. A strong peak at  $473\text{ cm}^{-1}$  was assigned to the stretching vibration of the Zn–O as shown in Fig. 6a–f

[48]. Figure 6b–c shows the stretching vibrations of epoxy C–O ( $1226.92\text{ cm}^{-1}$ ), and weak aromatic C=C ( $1560\text{ cm}^{-1}$ ) bands were observed from pure rGO and MWCNT [22, 49]. The basal plane of rGO consists of many p-conjugated aromatic domains which in





**Fig. 6** FT-IR spectra of (a) ZnO, (b) rGO, (c) MWCNT, (d) ZnO/rGO, (e) ZnO/MWCNT and (f) ZMG NCs

theory can strongly interact with the surface of MWCNTs through p–p attractions with ZnO and ZMG NCs. On the other hand, the peaks at  $3360\text{ cm}^{-1}$  and  $1655\text{ cm}^{-1}$  attributed to the vibration of the stretching and banding modes of hydroxyl (OH) group. Since the intensity of the ZnO characteristic peak is decreased, while the incorporation of the rGO and MWCNT content confirms the formation of ZMG NCs.

### 3.7 UV–Vis DRS analysis

The optical absorbance properties of the prepared catalysts were characterized by UV–Vis diffused reflectance spectroscopy (UV–Vis DRS) technique. The UV–Vis DRS spectra of cauliflower-shaped ZnO, ZnO/rGO, ZnO/MWCNT and ZMG NCs are shown in Fig. 7. Figure 7a illustrates the absorption peaks of 365 nm, 377 nm, 379 nm and 383 nm for the cauliflower-shaped ZnO, ZnO/rGO, ZnO/MWCNT, ZMG NCs, respectively [50]. The optical absorbance spectrum of ZMG lies below 400 nm that describes absorption in the ultraviolet region. With the formation of a ternary nanocomposites, the absorbance was slightly shifted toward greater absorption and the absorbance edge was shifted to the visible region (red shift). This recommends that surface of the binary metal oxide enhanced the absorption properties of the ZMG NCs and might be the reason for better catalytic activity of ZMG photocatalysts under UV–visible light. This supports the qualitative observation of a red shift in the absorption edge of ZMG NCs

compared to bare cauliflower-shaped ZnO. Furthermore, the band gap could be calculated from the Tauc plot  $(\alpha h\nu)^2$  versus photon energy  $(h\nu)$  for the direct energy gap semiconductor [51, 52] presented in Fig. 7b. Based on the Tauc plot, the calculated optical band gaps were 3.17 eV, 3.12 eV, 3.05 eV and 2.89 eV corresponding to cauliflower-shaped ZnO, ZnO/rGO, ZnO/MWCNT and ZMG NCs, respectively. The band gap was red shifted in the absorption edge of ZMG NCs compared to bare cauliflower-shaped ZnO [53]. It can be clearly seen that the absorbance ability to tune the band gap with the amount of MWCNT content dissolved in GO. MWCNT content in the GO matrix shows higher sensitivity due to the higher tunneling effect between the neighboring tubes, and the shrinkage of the rGO band gap helps in enhancing light absorption capability. The reduction in the bandgap phenomenon of ZMG NCs could be attributed to synergistic effect of ZnO, rGO and MWCNT.

The effective charge transfer properties of ZnO, ZnO/rGO, ZnO/MWCNT, and ZMG NCs composite were investigated by PL spectroscopy (Fig. S2). Three main emission peaks were observed in the ZnO cauliflower flower nanostructure (UV excitation wavelength 325 nm), which can be attributed to the recombination of photogenerated electron–hole pairs (peak at 390 nm), impurities, and structural defects (peak at 415 nm), and oxygen/zinc interstitials (peak located at 510 nm). On the other hand, ZMG NCs composites show a significant decrease in PL intensity compared to ZnO/rGO, ZnO/MWCNT, and ZnO catalysts, respectively. The synergistic effect between ZnO, MWCNT, and rGO nanosheets due to effectively reduces the recombination of the electron–hole pair and facilitates the charge carrier separation.

### 3.8 Photoelectrochemical measurements

The photo-induced charge separation and electron–hole recombination rate of the samples were measured by transient photocurrent (i-t) and electrochemical impedance spectroscopy (EIS). Figure 8a shows the transient photocurrent response of the cauliflower-shaped ZnO, ZnO/rGO, ZnO/MWCNT, and ZMG electrodes with several simulated sunlight on–off cycles. In general, photocurrent response maximum due to the efficient electron–hole separation improved photocatalytic activity. By adding MWCNTs, the light response was considerably

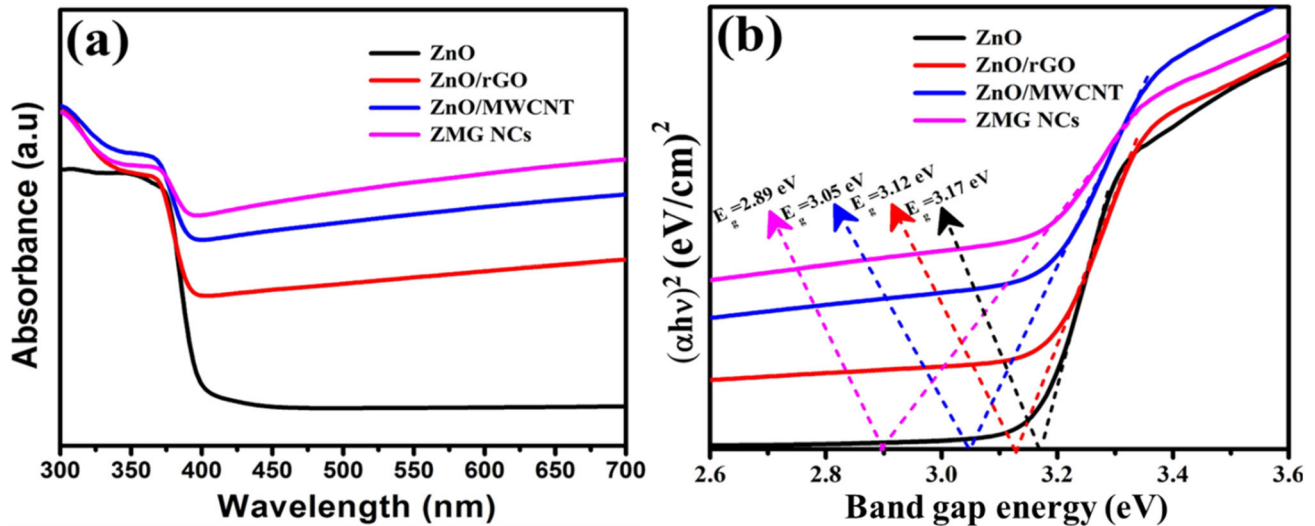


Fig. 7 UV-Vis DRS spectra of **a** cauliflower-shaped ZnO, ZnO/rGO, ZnO/MWCNT, ZMG NCs and **b** band gap energy

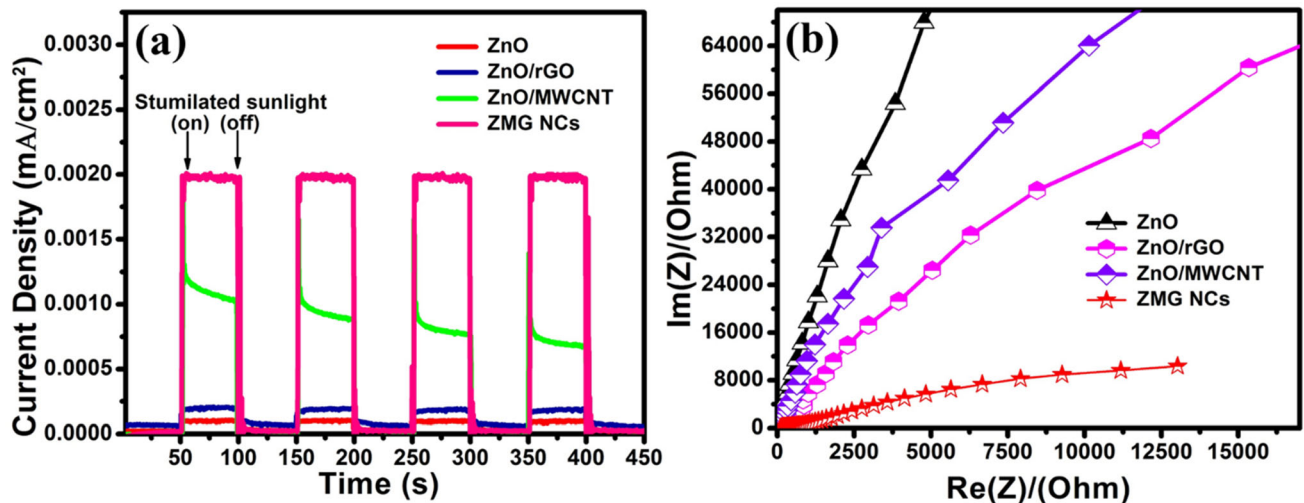


Fig. 8 **a** Photocurrent (i-t) curve of cauliflower-shaped ZnO, ZnO/rGO, ZnO/MWCNT and ZMG NCs and **b** EIS Nyquist plots for cauliflower-shaped ZnO, ZnO/rGO, ZnO/MWCNT and ZMG NCs

increased to 7300 nm (about 50 times) which shows the current density of ZnO/MWCNTs higher than ZnO/rGO. The photocurrent densities are  $19.1 \mu\text{A}/\text{cm}^2$ ,  $10.8 \mu\text{A}/\text{cm}^2$ ,  $2.2 \mu\text{A}/\text{cm}^2$ ,  $1.265 \mu\text{A}/\text{cm}^2$  and  $0.065 \mu\text{A}/\text{cm}^2$  corresponding to ZMG NCs, ZnO/MWCNT, ZnO/rGO and cauliflower-shaped ZnO, respectively. The ZMG NCs exhibited the highest photocurrent density ( $19.1 \mu\text{A}/\text{cm}^2$ ), which is about nineteen times higher than of the ZnO, and nine times higher than of the ZnO/rGO and two times higher than of the ZnO/MWCNT. These results are attributed to the synergistic effect of ZnO, MWCNT, and rGO in the composites [54]. Figure 8b

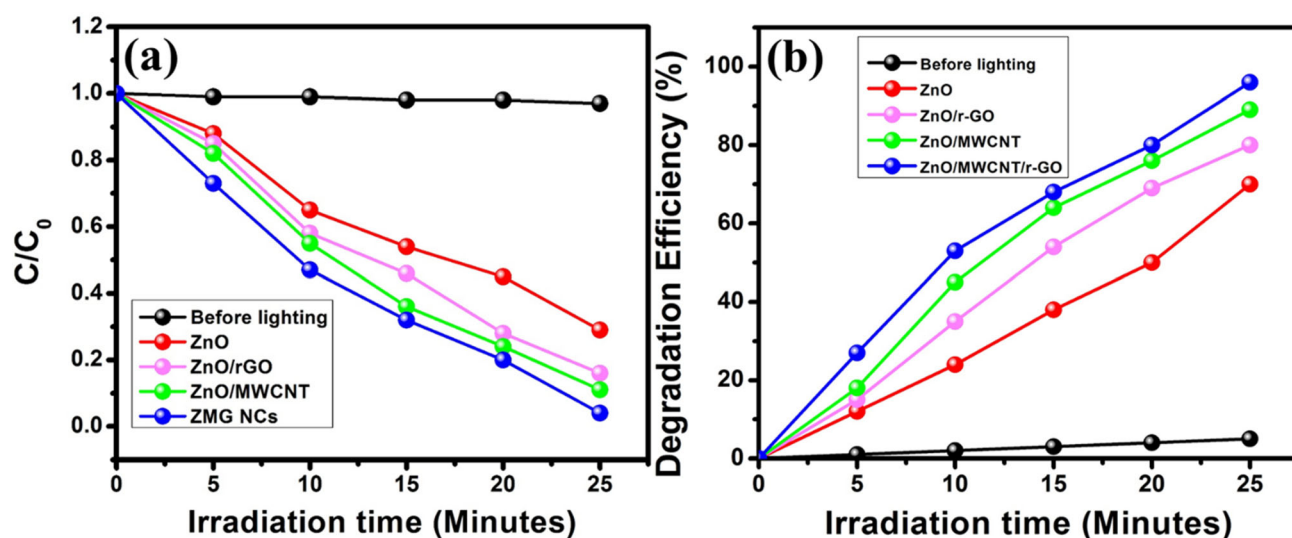
shows the EIS Nyquist plot of cauliflower-shaped ZnO, ZnO/rGO, ZnO/MWCNT, and ZMG NCs samples. The EIS Nyquist plot (arc) indicates the charge transfer resistance of electrode/electrolyte interfaces. The EIS Nyquist plot of ZMG NCs samples exhibits the lowest arc with the lower resistance and hence higher charge transfer properties. These results indicate that the ZMG NCs displays a high charge separation and high electron transfer properties, which is conformed to the photocurrent (i-t) measurements [55].

### 3.9 Photocatalytic activity

The photocatalytic activity of cauliflower-shaped ZnO, ZnO/rGO, ZnO/MWCNT, and ZMG NCs was evaluated through the degradation of methylene blue dye in aqueous solution. In the typical experiment, 100 mg of as-prepared ZnO nanoparticles was dispersed in 100 mL aqueous solution of MB with an initial concentration of 10 mg/L under ambient condition and it is continuously stirred under the dark condition for 1 h to reach adsorption–desorption equilibrium. In the adsorption–desorption experiment approximately 3% of dye adsorption occurred for 25 min of reaction. After that, the mixture was irradiated by halogen lamp in the photocatalytic experiment. The MB solution was taken after various exposure times (5 min), and UV–Vis spectra of ZnO, ZnO/rGO, ZMG NCs are shown in Fig. S3. Figure 9a shows the photocatalytic degradation rate of MB dye with before lighting, cauliflower-shaped ZnO, ZnO/rGO, ZnO/MWCNT, and ZMG NCs under visible irradiation. The degradation efficiency was calculated using Eq. (1), and the values are 71.9%, 79.6%, 86.01% and 96.3% (Fig. 9b) corresponding to cauliflower-shaped ZnO, ZnO/rGO, ZnO/MWCNT and ZMG NCs, respectively. Figure S4 shows the photodegradation rate, photocatalytic efficiency, photocurrent ( $i$ - $t$ ) curve, and EIS Nyquist plots of ZnO nanorods. The reaction rate constant of ternary nanocomposites was much greater than the bare and binary catalysts, respectively. Therefore, it conforms that the

composition of ZMG NCs significantly raised the photocatalytic activity of bare materials under the simulated light irradiation. The maximum degradation efficiency (96.3%) of the ZMGNCs could be attributed to the decreased bandgap of the composite, lower recombination rate, and the longer lifetime of the photogenerated electron–hole pairs [56]. This result indicates that it has a great potential application of MB dye degradation. The photocatalytic activity of as-prepared ZMG nanocomposites was compared to the previously reported different light activity of various nanocomposites as shown in Table 1. From Table 1, it is clear that the ZMG NCs nanocomposites materials showed enhanced activity compared to the previously reported other composites.

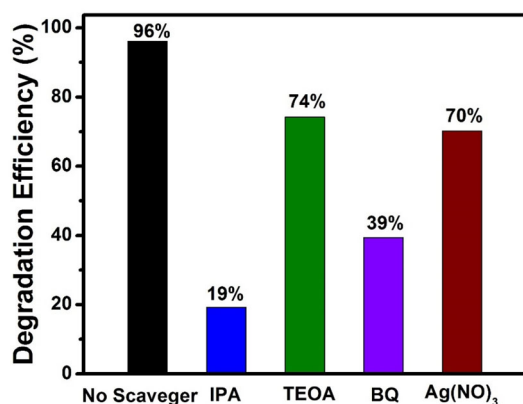
In order to investigate the active species of the photocatalytic process, the same experimental procedure of dye degradation was used. In these experiments, there was addition of 1 mM of IPA, TEOA, BQ, and AgNO<sub>3</sub>, respectively. Figure 10 shows the ZMG NCs degradation efficiency of 96%, 74%, 19%, 39%, 70% for the without scavengers, •OH (IPA), h<sup>+</sup> (TEOA), O<sup>2-</sup> (BQ) and e<sup>-</sup> (AgNO<sub>3</sub>), respectively [63]. The degradation efficiency decreased from 96 to 19% for the without and IPA scavengers under UV–Vis light irradiation in the presence of ZMG NCs. Moreover, the IPA had the lowest degradation efficiency (19%) where the •OH radicals act as a major role. The superoxide radicals



**Fig. 9** a Photodegradation rate of before lighting, cauliflower-shaped ZnO, ZnO/rGO, ZnO/MWCNT and ZMG NCs and b photocatalytic efficiency of cauliflower-shaped ZnO, ZnO/rGO, ZnO/MWCNT and ZMG NCs

**Table 1** Comparison of different light degradation rate (%) of dyes over previously reported binary and ternary heterojunction

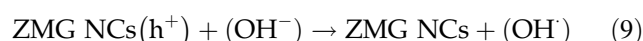
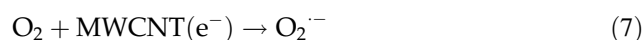
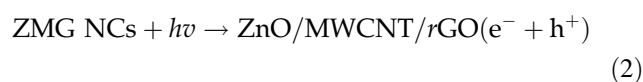
| S. No | Catalyst           | Catalyst mass (mg/L) | Dye | Light and intensity  | Irradiation time (mins) | Degradation efficiency (%) | Refs         |
|-------|--------------------|----------------------|-----|----------------------|-------------------------|----------------------------|--------------|
| 1     | ZnO                | 50                   | MO  | UV lamp (1000 W)     | 30                      | 99.70                      | [57]         |
| 2     | ZnO/rGO            | 50                   | RhB | xenon lamp (300 W)   | 140                     | 97                         | [58]         |
| 3     | ZnO-GQD            | 400                  | MB  | natural sunlight     | 70                      | 95                         | [59]         |
| 4     | ZnO/C-dots         | 100                  | MB  | halogen lamp (500 W) | 30                      | 96                         | [60]         |
| 5     | ZnO/graphene       | 30                   | MB  | halogen lamp (400 W) | 90                      | 93                         | [61]         |
| 6     | ZnO/CNT            | 100                  | MG  | LED lamp (150 W)     | 60                      | 79                         | [62]         |
| 7     | ZnO with MWCNT/rGO | 1000                 | MB  | Halogen lamp (250 W) | 25                      | 96                         | Present work |

**Fig. 10** Photocatalytic trapping experiment on ZMG NCs

(O<sup>2-</sup> (BQ)) are the secondary active species (39%). Moreover, in the presence of reactive species (O<sup>2-</sup>, h<sup>+</sup>, and e<sup>-</sup>) in the MB dye degradation process, the ZMG NCs were not dramatically decreased which is a minor role in the photocatalytic reaction system [51, 64].

Figure 11 illustrates the proposed photocatalytic reaction mechanism of ZMG NCs with MB dye solution under UV-Vis light irradiation. In the UV-Vis light (hν) was illuminated by the surface of ZMG NCs, and photon energy (hν) should be at least equal or more than the valence band energy of the ZnO nanostructures. The observed photon energy of the ZnO nanostructure was generated into photo-excited electrons and hole pairs. These photo-excited electrons may be transferred from the valence band (VB) to the conduction band (CB), and holes stay in the valence band (VB) of ZnO surfaces [65]. The photo-

excited electrons (ZnO surface) can be transferred from the CB into the surface of MWCNT and rGO, which is photogenerated electron-hole pair recombination suppressed. Moreover, the photo-generated electrons and holes can be generated active species and reacted with dye molecules to convert the water, oxygen, carbon dioxide, and excess of the electron [66]. The possible photocatalytic reactions are as follows:



### 3.10 Reusable test

The practical application of the prepared ZMG NCs was studied by the stability test. The ZMG catalyst was effectively reused for five cycles, and the degradation efficiency is seen in Fig. 12a. The dye degradation efficiency was a small deviation of the

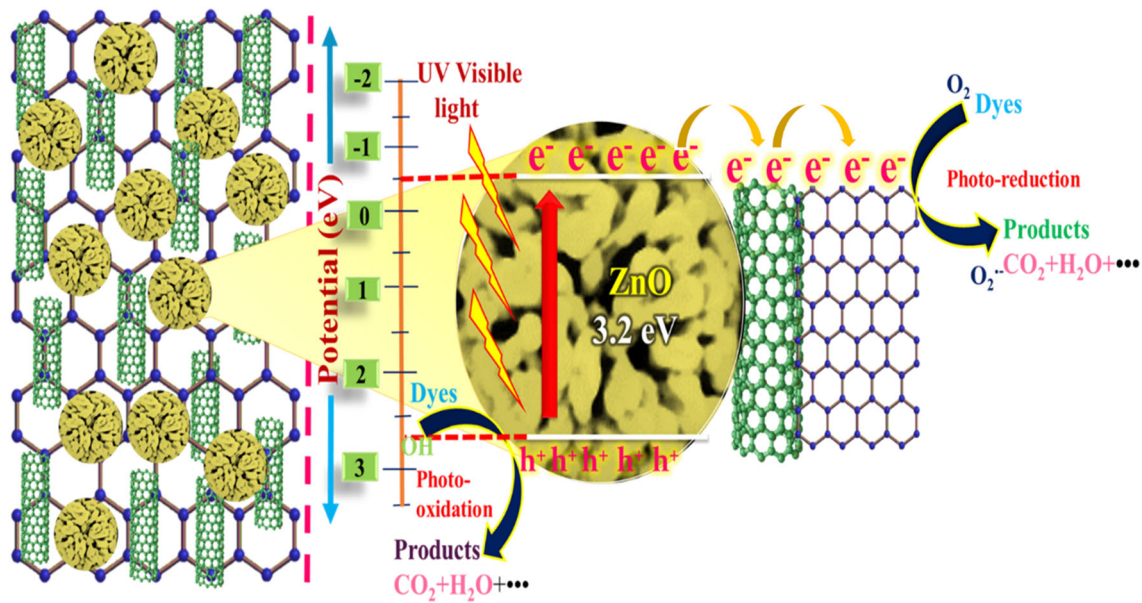


Fig. 11 Schematic diagram of photocatalytic mechanism (ZMG composite) during the dye degradation process [26, 67, 68]

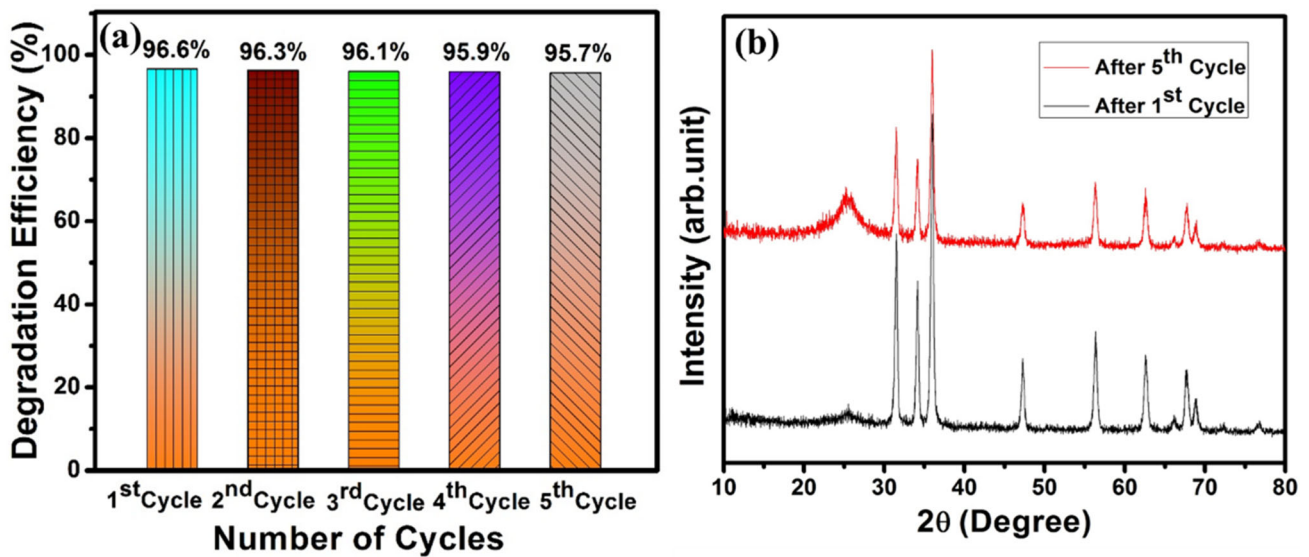


Fig. 12 Recycle degradation efficiency for a ZMG nanocomposite under MB dye with five cycles, b XRD pattern of recycle test for ZMG nanocomposite after first and fifth cycle

first cycle (96.3%) and the fifth cycle (95.7%) of reuse experiments [50]. The reusability test of the ZMG nanocomposite was investigated by the XRD pattern shown in Fig. 12b. The XRD patterns of first and fifth cycles show no change in the crystalline structure and phase purity of the prepared catalyst. The results indicate the enhanced photostability of the ZMG NCs, which is practically applicable in wastewater treatment.

#### 4 Conclusion

In summary, the ZMG NCs were successfully prepared by the facile hydrothermal method. The FE-SEM and TEM results have visualized the contact between cauliflower-shaped ZnO, MWCNT, and rGO sheets. The calculated band gap and surface area of the ZMG NCs correspond to 2.89 eV, and (45.877 m<sup>2</sup> g<sup>-1</sup>), respectively. In UV-Vis DRS and BET results, ZMG NCs exhibited reduced bandgap and

high surface area, which was charge transferred from ZnO into MWCNT, rGO and it reduces the charge recombination rate and enhanced photocatalytic activity of MB dye degradation. The photocurrent response of the ZMG NCs shows the highest photocurrent density ( $19.1 \mu\text{A}/\text{cm}^2$ ), which is charge transportation, separation, and suppressed charge carriers recombination and enhancement of the light absorption. Meanwhile, recycle stability (five cycles) of the ZMG NCs exhibited excellent photostability against photocorrosion. Therefore, the obtained product of ZMG NCs could be employed as a promising photocatalyst materials for practical applications in organic pollutant management.

**Supplementary Information:** The online version contains supplementary material available at <http://doi.org/10.1007/s10854-021-06129-5>.

## References

- M.A. Ashraf, M.M. Hanfiah, *Environ. Sci. Pollut. Res.* **24**, 22753 (2017)
- N. Ferronato, V. Torretta, *Int. J. Environ. Res. Public Health* **16**, 1060 (2019)
- S. Bolisetty, M. Peydayesh, R. Mezzenga, *Chem. Soc. Rev.* **48**, 463 (2019)
- K. Saruchi, V. Kumar, B.S. Kaith, R. Jindal, *Ind. Eng. Chem. Res.* **55**, 10492 (2016)
- M. Ghanbari, D. Emadzadeh, W.J. Lau, T. Matsuura, A.F. Ismail, *RSC Adv.* **5**, 21268 (2015)
- E.H. Umukoro, M.G. Peleyeju, J.C. Ngila, O.A. Arotiba, *RSC Adv.* **6**, 52868 (2016)
- M. Ranjeh, F. Beshkar, M. Salavati-Niasari, *Compos. Part B Eng.* **172**, 33 (2019)
- S. Prabhu, S. Megala, S. Harish, M. Navaneethan, P. Maadeswaran, S. Sohila, R. Ramesh, *Appl. Surf. Sci.* **487**, 1279 (2019)
- F. Namvar, F. Beshkar, M. Salavati-Niasari, S. Bagheri, *J. Mater. Sci. Mater. Electron.* **28**, 10313 (2017)
- S. Prabhu, M. Pudukudy, S. Sohila, S. Harish, M. Navaneethan, D. Navaneethan, R. Ramesh, Y. Hayakawa, *Opt. Mater. (Amst.)* **79**, 186 (2018)
- M. Ranjeh, F. Beshkar, O. Amiri, M. Salavati-Niasari, H. Moayedi, *J. Alloys Compd.* **815**, 152451 (2020)
- M. Valian, F. Beshkar, M. Salavati-Niasari, *J. Mater. Sci. Mater. Electron.* **28**, 12440 (2017)
- N. Rosman, W.N.W. Salleh, M.A. Mohamed, Z. Harun, A.F. Ismail, F. Aziz, *Sep. Purif. Technol.* **251**, 117391 (2020)
- M.A. Mohamed, M.F.M. Zain, L. Jeffery Minggu, M.B. Kassim, J. Jaafar, N.A. Saidina Amin, M.S. Mastuli, H. Wu, R.J. Wong, Y.H. Ng, *J. Ind. Eng. Chem.* **77**, 393 (2019)
- S. Luo, C. Liu, Y. Wan, W. Li, C. Ma, S. Liu, H. Jan Heeres, W. Zheng, K. Seshan, S. He, *Appl. Surf. Sci.* **513**, 145878 (2020)
- N. Zhang, Y. Zhang, Y.J. Xu, *Nanoscale* **4**, 5792 (2012)
- C. Gu, S. Xiong, Z. Zhong, Y. Wang, W. Xing, *RSC Adv.* **7**, 22234 (2017)
- L.L. Zhang, Z. Xiong, X.S. Zhao, *ACS Nano* **4**, 7030 (2010)
- M. Shams, L.M. Guiney, L. Huang, M. Ramesh, X. Yang, M.C. Hersam, I. Chowdhury, *Environ. Sci. Nano* **6**, 2203 (2019)
- M.A. Mohamed, W.N. Wan Salleh, J. Jaafar, M.S. Rosmi, Z.A. Zul, M. Abd Mutalib, A.F. Ismail, M. Tanemura, *Appl. Surf. Sci.* **393**, 46 (2017)
- M.A. Mohamed, W.N.W. Salleh, J. Jaafar, A.F. Ismail, N.A.M. Nor, *Mater. Chem. Phys.* **162**, 113 (2015)
- H. Yao, F. Li, J. Lutkenhaus, M. Kotaki, H.J. Sue, *AIMS Mater. Sci.* **3**, 1410 (2016)
- Y. Chen, H. Ge, L. Wei, Z. Li, R. Yuan, P. Liu, X. Fu, *Catal. Sci. Technol.* **3**, 1712 (2013)
- Z. Chen, N. Zhang, Y.J. Xu, *CrystEngComm* **15**, 3022 (2013)
- A. Shanmugasundaram, R. Boppella, Y.J. Jeong, J. Park, Y.B. Kim, B. Choi, S.H. Park, S. Jung, D.W. Lee, *Mater. Chem. Phys.* **218**, 218 (2018)
- D. Shao, H. Sun, J. Gao, G. Xin, M. Anthony Aguilar, T. Yao, N. Koratkar, J. Lian, S. Sawyer, *Nanoscale* **6**, 13630 (2014)
- T.A. Saleh, M.A. Gondal, Q.A. Drmash, *Nanotechnology* **21**, 495705 (2010)
- M.M.H. Farooqi, R.K. Srivastava, *Optik (Stuttg.)* **127**, 3991 (2016)
- Z. Kalantari Bolaghi, S.M. Masoudpanah, M. Hasheminasari, *Mater. Res. Bull.* **115**, 191 (2019)
- S. Demirci, T. Dikici, M.M. Tünçay, N. Kaya, *Appl. Surf. Sci.* **507**, 145083 (2020)
- D.S. Ahmed, M.R. Mohammed, M.K.A. Mohammed, *Nanosci. Nanotechnol-Asia* **10**, 127 (2020)
- S. Prabhu, M. Pudukudy, S. Harish, M. Navaneethan, S. Sohila, K. Murugesan, R. Ramesh, *Mater. Sci. Semicond. Process.* **106**, 104754 (2020)
- Y. Mao, Y. Li, Y. Zou, X. Shen, L. Zhu, G. Liao, *Ceram. Int.* **45**, 1724 (2019)
- A. Muthukrishnaraj, S.S. Kalaivani, A. Manikandan, H.P. Kavitha, R. Srinivasan, N. Balasubramanian, *J. Alloys Compd.* **836**, 155377 (2020)
- G.K. Upadhyay, J.K. Rajput, T.K. Pathak, V. Kumar, L.P. Purohit, *Vacuum* **160**, 154 (2019)

36. G.K. Upadhyay, J.K. Rajput, T.K. Pathak, P.K. Pal, L.P. Purohit, *Appl. Surf. Sci.* **509**, 145326 (2020)
37. N. Duraisamy, K. Kandiah, R. Rajendran, S. Prabhu, R. Ramesh, G. Dhanaraj, *Res. Chem. Intermed.* **44**, 5653 (2018)
38. P. Arumugam, P. Sengodan, N. Duraisamy, R. Rajendran, V. Vasudevan, *Ionics (Kiel)*. **26**, 4201 (2020)
39. M. Azarang, A. Shuhaimi, M. Sookhikian, *RSC Adv.* **5**, 53117 (2015)
40. Y.J. Kwon, A. Mirzaei, S.Y. Kang, M.S. Choi, J.H. Bang, S.S. Kim, H.W. Kim, *Appl. Surf. Sci.* **413**, 242 (2017)
41. X. Jin, Z. Ma, G. Liu, D. Hu, C. Song, Q. Huang, *J. Environ. Chem. Eng.* **8**, 104030 (2020)
42. (n.d.).
43. F. Wang, Y. Zhou, X. Pan, B. Lu, J. Huang, Z. Ye, *Phys. Chem. Chem. Phys.* **20**, 6959 (2018)
44. Z.W. Wu, S.L. Tyan, H.H. Chen, J.C.A. Huang, Y.C. Huang, C.R. Lee, T.S. Mo, *Superlattices Microstruct.* **107**, 38 (2017)
45. S. Shilpa, B.M. Basavaraja, S.B. Majumder, A. Sharma, *J. Mater. Chem. A* **3**, 5344 (2015)
46. M.M. Lu, W.Q. Cao, H.L. Shi, X.Y. Fang, J. Yang, Z.L. Hou, H.B. Jin, W.Z. Wang, J. Yuan, M.S. Cao, *J. Mater. Chem. A* **2**, 10540 (2014)
47. H. Moussa, E. Giroto, K. Mozet, H. Alem, G. Medjahdi, R. Schneider, *Appl. Catal. B Environ.* **185**, 11 (2016)
48. M. Pudukudy, Z. Yaakob, *Superlattices Microstruct.* **63**, 47 (2013)
49. S. Barthwal, B. Singh, S. Barthwal, N.B. Singh, *Sens. Lett.* **15**, 955 (2018)
50. Y. Peng, J. Ji, D. Chen, *Appl. Surf. Sci.* **356**, 762 (2015)
51. A. Priyadharsan, S. Shanavas, V. Vasanthakumar, B. Balamuralikrishnan, P.M. Anbarasan, *Colloids Surf. A Physicochem. Eng.* **559**, 43 (2018)
52. A. Priyadharsan, S. Shanavas, C. Vidya, J. Kalyana Sundar, R. Acevedo, P.M. Anbarasan, *Mater. Today Proc.* **26**, 3522 (2020)
53. H.N. Tien, V.H. Luan, L.T. Hoa, N.T. Khoa, S.H. Hahn, J.S. Chung, E.W. Shin, S.H. Hur, *Chem. Eng. J.* **229**, 126 (2013)
54. R. Vinoth, P. Karthik, C. Muthamizchelvan, B. Neppolian, M. Ashokkumar, *Phys. Chem. Chem. Phys.* **18**, 5179 (2016)
55. W. He, R. Wang, L. Zhang, J. Zhu, X. Xiang, F. Li, *J. Mater. Chem. A* **3**, 17977 (2015)
56. Q.P. Luo, X.Y. Yu, B.X. Lei, H.Y. Chen, D. Bin Kuang, C.Y. Su, *J. Phys. Chem. C* **116**, 8111 (2012)
57. X. Chen, Z. Wu, D. Liu, Z. Gao, *Nanoscale Res. Lett.* **12**, 1–10 (2017)
58. Y. Zhao, L. Liu, T. Cui, G. Tong, W. Wu, *Appl. Surf. Sci.* **412**, 58 (2017)
59. S. Kumar, A. Dhiman, P. Sudhagar, V. Krishnan, *Appl. Surf. Sci.* **447**, 802 (2018)
60. A. Velumani, P. Sengodan, P. Arumugam, R. Rajendran, S. Santhanam, M. Palanisamy, *Curr. Appl. Phys.* **20**, 1176 (2020)
61. M. Ahmad, E. Ahmed, Z.L. Hong, J.F. Xu, N.R. Khalid, A. Elhissi, W. Ahmed, *Appl. Surf. Sci.* **274**, 273 (2013)
62. N. Arsalani, S. Bazazi, M. Abuali, S. Jodeyri, *J. Photochem. Photobiol. A Chem.* **389**, 112207 (2020)
63. J. He, C. Niu, C. Yang, J. Wang, X. Su, *RSC Adv.* **4**, 60253 (2014)
64. D. Hu, C. Song, X. Jin, Q. Huang, *J. Alloys Compd.* **843**, 156030 (2020)
65. P. Riente, T. Noël, *Catal. Sci. Technol.* **9**, 5186 (2019)
66. C. Zhang, J. Zhang, Y. Su, M. Xu, Z. Yang, Y. Zhang, *Phys. E Low-Dimens. Syst. Nanostruct.* **56**, 251 (2014)
67. L. Fu, G. Lai, H. Zhang, A. Yu, *J. Nanosci. Nanotechnol.* **15**, 4325 (2015)
68. D. Chaudhary, S. Singh, V.D. Vankar, N. Khare, *J. Photochem. Photobiol. A Chem.* **351**, 154 (2018)

**Publisher's Note** Springer Nature remains neutral with regard to jurisdictional claims in published maps and institutional affiliations.